Materials Advances

ROYAL SOCIETY OF CHEMISTRY

PAPER

View Article Online
View Journal | View Issue

Cite this: *Mater. Adv.*, 2024, 5, 2898

Pliable electrode of porous graphene-encapsulated $FeNiSe_4$ binary-metal selenide nanorods as a binder-free anode for lithium-ion batteries†

Mingming Hao, Caiyun Guo, Yuhui Wen, Liting Zhao, Xiaoting Zhang * and Rui Wang*

Porous graphene-encapsulated $FeNiSe_4$ binary-metal selenide nanorods ($FeNiSe_4$@PG) were prepared by filtration, annealing, and selenylation techniques. The morphology and structure of $FeNiSe_4$@PG were investigated by scanning electron microscopy (SEM), transmission electron microscopy (TEM), selected area electron diffraction (SAED), and X-ray diffraction (XRD). The interfacial interaction of $FeNiSe_4$ and graphene was characterized using X-ray photoelectron spectroscopy (XPS) and Raman spectroscopy. $FeNiSe_4$@PG exhibited excellent electrochemical performance when used as an anode for lithium-ion batteries. The first reversible capacity of $FeNiSe_4$@PG at 100 mA g^{-1} was 861.0 mA h g^{-1} and increased to 1121.6 mA h g^{-1} after 50 cycles. Even at 1, 2, and 5 A g^{-1}, the specific capacities could still maintain 610.3, 314.1, and 144.4 mA h g^{-1}, even after 500 cycles, respectively. The excellent electrochemical performance of $FeNiSe_4$@PG should be attributed to its special structure. First, the excellent electrical conductivity of graphene improved the overall electrical property of the electrode material. Second, the porous structure of graphene facilitated the infiltration of the electrolyte into the film electrode. Moreover, the synergistic effect of iron and nickel in $FeNiSe_4$@PG and the strong interfacial interaction between graphene and $FeNiSe_4$ contributed to the rapid diffusion of lithium ions and the transport of electrons.

Received 27th October 2023,
Accepted 5th February 2024

DOI: 10.1039/d3ma00911d

rsc.li/materials-advances

Introduction

The rapid development of the economy is inseparable from the strong support of the energy supply. Fossil fuels with limited reserves and heavy pollution are still dominant sources of energy. Based on the strategic consideration of sustainable development, the development of renewable clean energy is urgent.[1] Lithium-ion batteries (LIBs) are preferred due to the advantages of high energy density and operating voltage.[2–5] As an important component of the battery, electrode materials play a crucial role in the electrochemical performance of LIBs. However, graphite, the current commercial anode material, limits the further improvement of the energy density of LIBs due to its low theoretical specific capacity.[6] Different from the intercalation mechanism of carbon materials, transition metal compounds usually exhibit a conversion mechanism, which has higher theoretical specific capacities. Compared with metal oxides and sulfides, metal selenides have a lower band gap and higher covalent state, higher electrical conductivity, higher stack density, and better electrochemical activity.[7–10] In addition, the metal–Se covalent bonds are weaker and the d-electron arrangement is proper.[11–13] $FeSe_2$,[14–16] $CoSe_2$,[17–19] and $NiSe_2$[11,20,21] have attracted considerable attention due to their large interlayer distances, high theoretical specific capacity, and low cost.[22,23] For example, Chen *et al.* designed bamboo-like N-doped carbon nanotube encapsulated $FeSe_2$ nanoparticles *via* self-catalysis and chemical transformation, and the material exhibited excellent electrochemical performance when used as an anode material for

Beijing Key Laboratory of Clothing Materials R & D and Assessment, Beijing Engineering Research Center of Textile Nanofiber, School of Materials Design & Engineering, Beijing Institute of Fashion Technology, Beijing 100029, China. E-mail: zhangxt@bift.edu.cn, clywangrui@bift.edu.cn

† Electronic supplementary information (ESI) available: The SEM images of Ni/PG and $NiSe_2$/PG. The XRD pattern of FeNi@PG. The C1s spectrum of $FeNiSe_4$@PG. The XPS spectrum of $NiSe_2$/PG. Raman spectra of $NiSe_2$/PG and $FeNiSe_4$@PG. The electrochemical performance of $FeSe_2$/PG. The TG curves of $FeNiSe_4$@PG, $NiSe_2$/PG, and $FeSe_2$/PG. The SEM images of $FeNiSe_4$@PG, $NiSe_2$/PG, and $FeSe_2$/PG electrodes after cycling. The SEM images of $FeNiSe_4$@PG electrodes after cycling at different current densities. The relationship between Z' and $\omega^{-1/2}$ for $FeNiSe_4$@PG, $NiSe_2$/PG, and $FeSe_2$/PG. The CV curves at various sweep rates and corresponding log(peak current)–log(sweep rate) plots for $FeNiSe_4$@PG electrode. The pseudocapacitive contributions for the $FeNiSe_4$@PG electrode at various sweep rates. The pseudocapacitive and diffusion-controlled contribution for the $FeNiSe_4$@PG electrode at 1.2 mV s^{-1}. The full battery performance of $FeNiSe_4$@PG. The AC impedance resistance of $NiSe_2$/PG and $FeNiSe_4$@PG. See DOI: **https://doi.org/10.1039/d3ma00911d**

LIBs.[14] Chen *et al.* synthesized novel $CoSe_2/Ti_3C_2T_x$ composites by growing $CoSe_2$ particles *in situ* on $Ti_3C_2T_x$ *via* a hydrothermal method and showed high specific capacities and good stability.[18] Sun *et al.* prepared $NiSe_2$/multi-heteroatom doped carbon/reduced graphene oxide, which exhibited excellent electrochemical properties, especially cycling stability.[21]

Compared to mono-metal selenides, binary-metal selenides have larger crystal sizes, more electroactive centers, and lower activation energy for electron transfer among cations. Thus, they exhibit more excellent electrical conductivity.[24–27] Moreover, binary-metal selenides have a synergistic effect between the two metals and expose more active sites for electrochemical reactions.[28–31] In addition, the binary-metal selenides have faster lithium-ion diffusion kinetics and can increase the reversible capacity and prolong the cycle life.[28] Since the atomic radii of Fe and Ni are similar, the bimetallic selenides of iron and nickel contribute to the compatibility of the crystalline structure.[32] The orbital overlap between the elements of iron, nickel, and selenium makes each atom have a more stable atomic interaction and improves the stability of the anode material.[30] However, to the best of our knowledge, the iron and nickel bimetallic selenides ($FeNiSe_4$) as the anode for LIBs have not yet been explored previously.

Similar to mono-metallic selenides, bimetallic selenides also face serious volume changes during the charge/discharge process in the practical application of the anode materials, which leads to rapid capacity decay and cycle performance deterioration.[33–35] In addition, the electrical conductivity of the binary-metal (Fe and Ni) selenide still cannot meet the requirements of the electrode material although the conductivity is better than that of the other transition-metal chalcogenides. Due to the advantages of superior electronic conductivity and chemical stability, graphene can be used to alleviate the volume changes of binary-metal (Fe and Ni) selenide and improve its conductivity.[36,37] In addition, the current mainstream electrode preparation involves a coating process using insulating binders, which can limit electron transport and ion diffusion and decrease the energy density of batteries due lack of capacity contribution.[38,39] Thus, it is essential to design free-standing anode materials without binder.

In this work, we report a free-standing anode material $FeNiSe_4$ nanorods on porous graphene film *via* vacuum filtration, annealing, and selenylation processes. The high conductivity of graphene contributes to improving the conductivity of the electrode material. The porous structure facilitates the diffusion of lithium ions, the transport of electrons, and the infiltration of electrolytes. In addition, the synergistic effect of Fe and Ni is conducive to increasing the active sites of electrochemical reactions. Thus, when used as an anode material for LIBs, the $FeNiSe_4$ nanorods exhibit excellent electrochemical performance.

Experimental

Synthesis of $FeNiSe_4$@PG

$FeNiSe_4$@PG was prepared using hydrated ferric nitrate, hydrated nickel nitrate, graphene oxide, and selenium powder. Firstly, $Fe(NO_3)_3{\cdot}9H_2O$ (0.08 mmol), $Ni(NO_3)_2{\cdot}6H_2O$ (1.6 mmol) and graphene oxide (10 ml, 1 mg ml^{-1}) were mixed and sonicated for 30 min. Then, the mixture was maintained under vigorous stirring for 3 h and filtered through a membrane (0.22 mm pore size). After annealing at 1000 °C for 1 h in an argon gas atmosphere, FeNi@PG was obtained. Finally, the $FeNiSe_4$@PG was obtained after selenization using Se powders (0.6 g) at 410 °C for 6 h in H_2(15%)/Ar(85%) mixture gas atmosphere. Both $FeSe_2$/PG and $NiSe_2$/PG were prepared as control samples using the same procedure except for the addition of hydrated nickel nitrate or hydrated ferric nitrate.

Characterization

Scanning electron microscopy (SEM, JEOL JSM-7500F) and transmission electron microscopy (TEM, JEOL JEM-2100F) were used to investigate the morphology of the samples. X-ray diffraction (XRD, Rigaku D/max-2500B2+/PCX) and selected area electron diffraction (SAED) were used to characterize the structure of the obtained samples. X-ray photoelectron energy spectra (XPS) were used to characterize the interfacial interaction using a monochromatized Al Kα radiation (1486.6 eV) with 30 eV pass energy in 0.5 eV step over an area of 0.65 mm × 0.65 mm. Thermogravimetry (TG) was used to investigate the contents of graphene in the electrode materials. The samples were heated from room temperature to 700 °C at 5 °C min^{-1} under an O_2 atmosphere.

Electrochemical measurements

The lithium-ion storage performance was studied using 2032 coin-type cells. $FeNiSe_4$@PG was directly used as the working electrode without any conductive additives and binders. The counter electrode, separator, and electrolyte were pure lithium sheet, polypropylene, and a solution of 1 M $LiPF_6$ in ethylene carbonate (EC)–diethyl carbonate (DEC) (1 : 1 by volume), respectively. The specific capacities, rate capability, and cycle performance were tested at various rates in the voltage range of 0.01–3.00 V using a Land battery test system (CT3001A, WUHAN LAND). The cyclic voltammograms (CV) were obtained at the range of 0.01–3.00 V with a scan rate of 0.1 mV s^{-1} using a CHI600E electrochemical working station (Shanghai Chenhua). The electrochemical impedance spectral (EIS) measurements were also carried out on a CHI600E electrochemical working station and the frequency range was from 10^5 Hz to 10^{-2} Hz.

Results and discussion

Fig. 1 shows the schematic of the forming process of $FeNiSe_4$@PG. First, hydrated ferric nitrate and nickel nitrate were dispersed into graphene oxide. Second, the graphene oxide/ferric nitrate/nickel nitrate composite film was obtained after ultrasonic, stirring, and vacuum filtration. Third, the composite film was converted into FeNi@PG under an Ar atmosphere. Finally, $FeNiSe_4$@PG was obtained after selenization of FeNi@PG.

The morphology of FeNi@PG showed that FeNi nanoparticles were located in the pores of the porous graphene film (Fig. 2a and b). The formation of the pores was due to the carbothermal reaction of ferric nitrate, nickel nitrate and

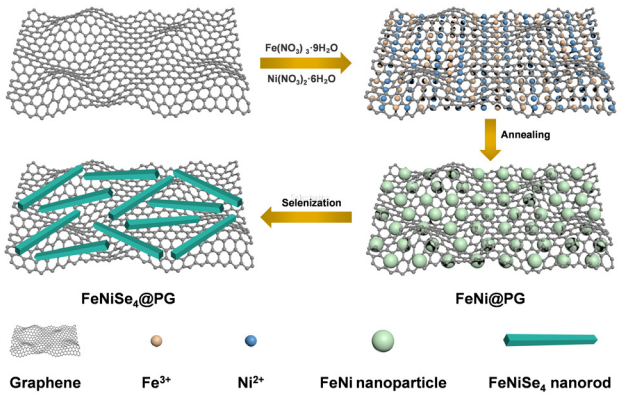

Fig. 1 Schematic diagram of the forming process of $FeNiSe_4$@PG.

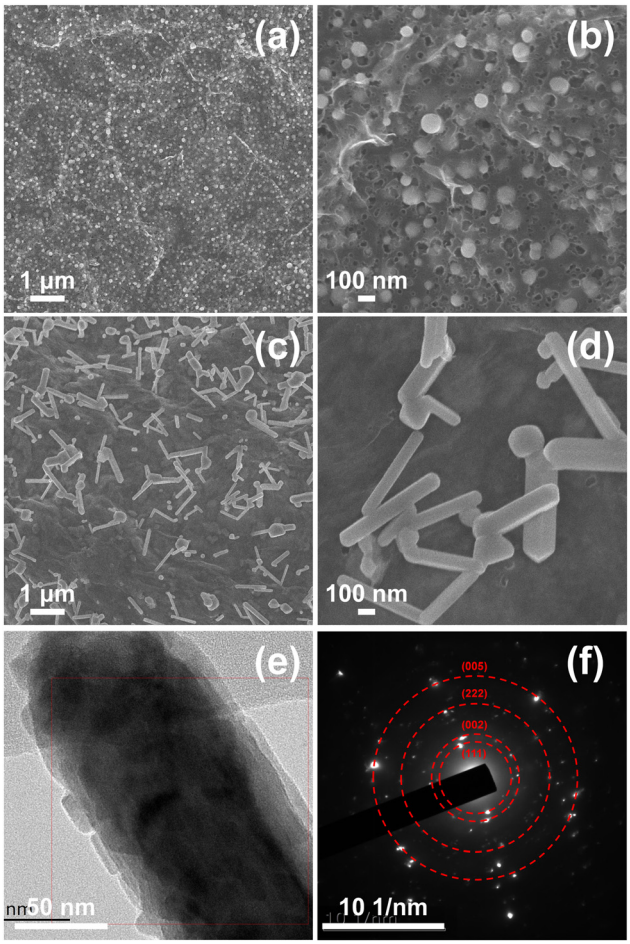

Fig. 2 SEM images of (a) and (b) FeNi@PG and (c) and (d) $FeNiSe_4$@PG, (e) TEM image of $FeNiSe_4$@PG and (f) corresponding SAED pattern.

graphene.[40–42] During annealing, carbon atoms reacted with metal ions and the porous structure was obtained. In addition, the functional groups on graphene oxide decomposed, and graphene was obtained. Interestingly, after selenization, the granular FeNi was transformed into nanorod-like $FeNiSe_4$ (Fig. 2c and d). The formation of nickel–iron selenide nanorods should be attributed to the Oriented Attachment (OA) mechanism.[43–45] It is worth noting that iron plays a decisive role in the formation of the nanorods. Previous reports have shown that when granular iron carbide is selenized under similar conditions, nanorod-like iron selenide can be easily obtained.[16] However, when granular nickel selenide is selenized, granular nickel selenide can still be obtained (Fig. S1, ESI†). Fig. 2f shows that the diffraction spots matching (111), (002), (222), and (005) diffraction rings in the selected area electron diffraction (SAED) image of $FeNiSe_4$@PG, indicating $FeNiSe_4$ nanorods are polycrystalline. The XRD pattern of $FeNiSe_4$@PG confirmed the existence of $FeNiSe_4$ in $FeNiSe_4$@PG, corresponding to the standard card JCPDS 97-063-2969 (Fig. 3 and Fig. S2, ESI†).

Fig. 4a shows the XPS spectra of $FeNiSe_4$@PG, which is composed of C, O, Fe, Ni, and Se elements. The curve fitting of C 1s, Fe 2p, Ni 2p, and Se 3d was carried out using a Gaussian–Lorentzian peak shape after a Shirley background correction. The C 1s spectra of $FeNiSe_4$@PG can be fitted to the C in the aromatic rings (285 eV), C in C–O (286.1 eV), and C in C═O (289 eV) (Fig. S3, ESI†).[46–48] For the Fe 2p spectrum of $FeNiSe_4$@PG, the peaks at 711.5, 724.8, 707.4, and 720.1 eV are ascribed to Fe^{3+} $2p_{3/2}$, Fe^{3+} $2p_{1/2}$, Fe^{2+} $2p_{3/2}$, and Fe^{2+} $2p_{1/2}$, respectively (Fig. 4b).[49–51] The Ni 2p peak of $FeNiSe_4$@PG can be fitted to six peaks. The peaks at 874.1 and 856.1 eV can be attributed to Ni^{3+} $2p_{1/2}$ and Ni^{3+} $2p_{3/2}$, respectively. The peaks at 871.1 and 853.7 eV should arise from Ni^{2+} $2p_{1/2}$ and Ni^{2+} $2p_{3/2}$, (Fig. 4c) and the corresponding satellite peaks are located at 878.8 and 860.3 eV respectively.[52–57] Interestingly, the Ni 2p spectrum of $FeNiSe_4$@PG presents upshifts to higher binding energies about 0.1 eV compared to that in $NiSe_2$/PG, indicating the synergistic effect of Fe and Ni in $FeNiSe_4$@PG changes the electrical structure of $NiSe_2$ and the charge transfer occurs from nickel and iron to selenium (Fig. S4, ESI†). For the Se 3d spectrum, the peaks at 56.5 and 59.3 eV could be ascribed to

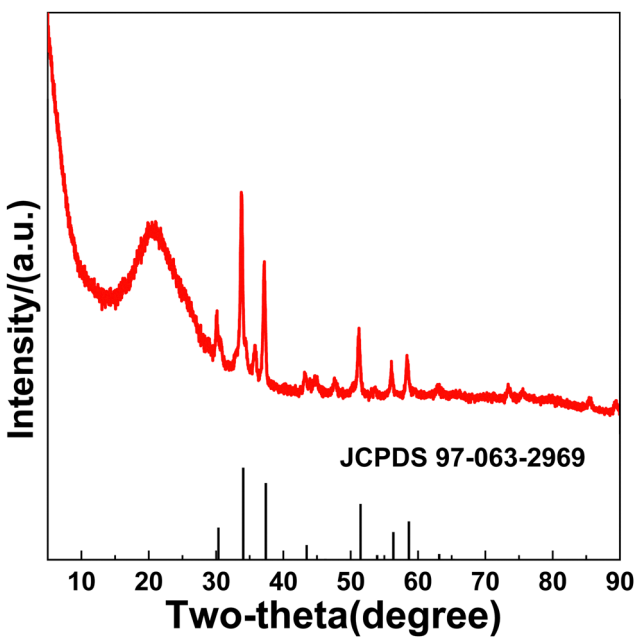

Fig. 3 XRD pattern of $FeNiSe_4$@PG.

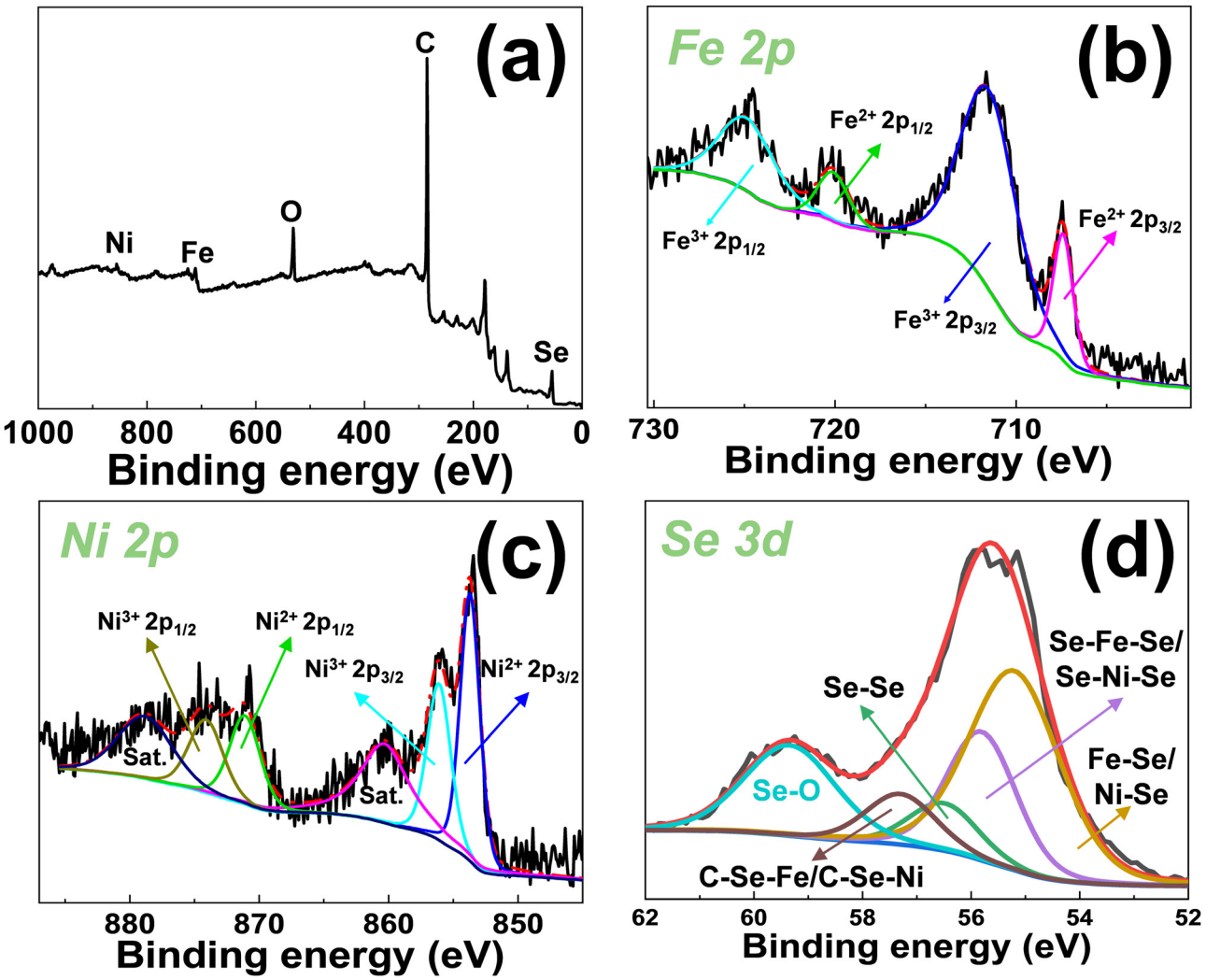

Fig. 4 (a) XPS spectrum of $FeNiSe_4$@PG and its (b) Fe 2p, (c) Ni 2p, and (d) Se 3d spectra.

Se–Se and Se–O, respectively. The peaks of 55.8 and 55.2 eV could come from the covalent bonds between selenium and iron/nickel.[55–57] The middle peak at 57.3 eV corresponds to the interfacial interaction between $FeNiSe_4$ and graphene,[42] indicating the formation of C–Se–Fe/C–Se–Ni bonds between graphene and $FeNiSe_4$. The Raman spectrum showed two characteristic peaks located at 1345 and 1585 cm^{-1}, corresponding to the D band and G band, respectively.[41] The I_D/I_G of $FeNiSe_4$@PG decreases to 0.94 from 1.14 ($NiSe_2$/PG), indicating the synergistic effect of Fe and Ni in $FeNiSe_4$@PG enhances the interfacial interaction between $FeNiSe_4$ and graphene (Fig. S5, ESI†).

To explore the electrochemical performance of $FeNiSe_4$@PG, the specific capacity, rate capability and cycle performance of $FeNiSe_4$@PG as anode materials for LIBs were evaluated by galvanostatic charge/discharge measurements under a voltage window of 0.01–3.00 V. Fig. 5a shows the cyclic voltammetry curves of $FeNiSe_4$@PG for the initial three cycles at a scan rate of 0.1 mV s^{-1}. In the CV curves, the first cathodic peak at 1.90 V during the discharge process should correspond to the intercalation of Li^+ into the $FeNiSe_4$@PG electrode. The peaks at 1.36 and 1.56 V can be ascribed to the lithiation reaction of $FeNiSe_4$ and Fe, Ni, and Li_2Se were generated. The peaks at 0.69 and 0.01 V should be attributed to the solid electrolyte interface (SEI) layers and the insertion of Li^+ into the graphene layers, respectively. During the second cathodic process, there are four cathodic peaks at 1.88, 1.69, 1.34, and 0.81 V during the discharge process, which are attributed to the multistep transformation of lithium and $FeNiSe_4$ to Fe, Ni, and Li_2Se.[31] The excellent overlapping of the third and second cycles indicates that the lithiation and delithiation are highly reversible. In the subsequent charging process, the two anodic peaks at 2.07 and 2.32 V correspond to the multistep delithiation reaction of Li_2Se.[58] Nickel and iron will react with Li_2Se and $FeNiSe_4$ was obtained (Fig. 5a).

The first discharge capacity and reversible capacity of $FeNiSe_4$@PG are 1125.5 and 861 mA h g^{-1} at 100 mA g^{-1}, respectively (Fig. 5b). However, the reversible capacities of $NiSe_2$/PG and $FeSe_2$/PG are only 479 and 507.9 mA h g^{-1}, respectively, at the same current density. The initial coulombic efficiency (ICE) of $FeNiSe_4$@PG can reach up to 76.5%, while the ICEs of $NiSe_2$/PG and $FeSe_2$/PG are only 62.2% and 64%, respectively. On the

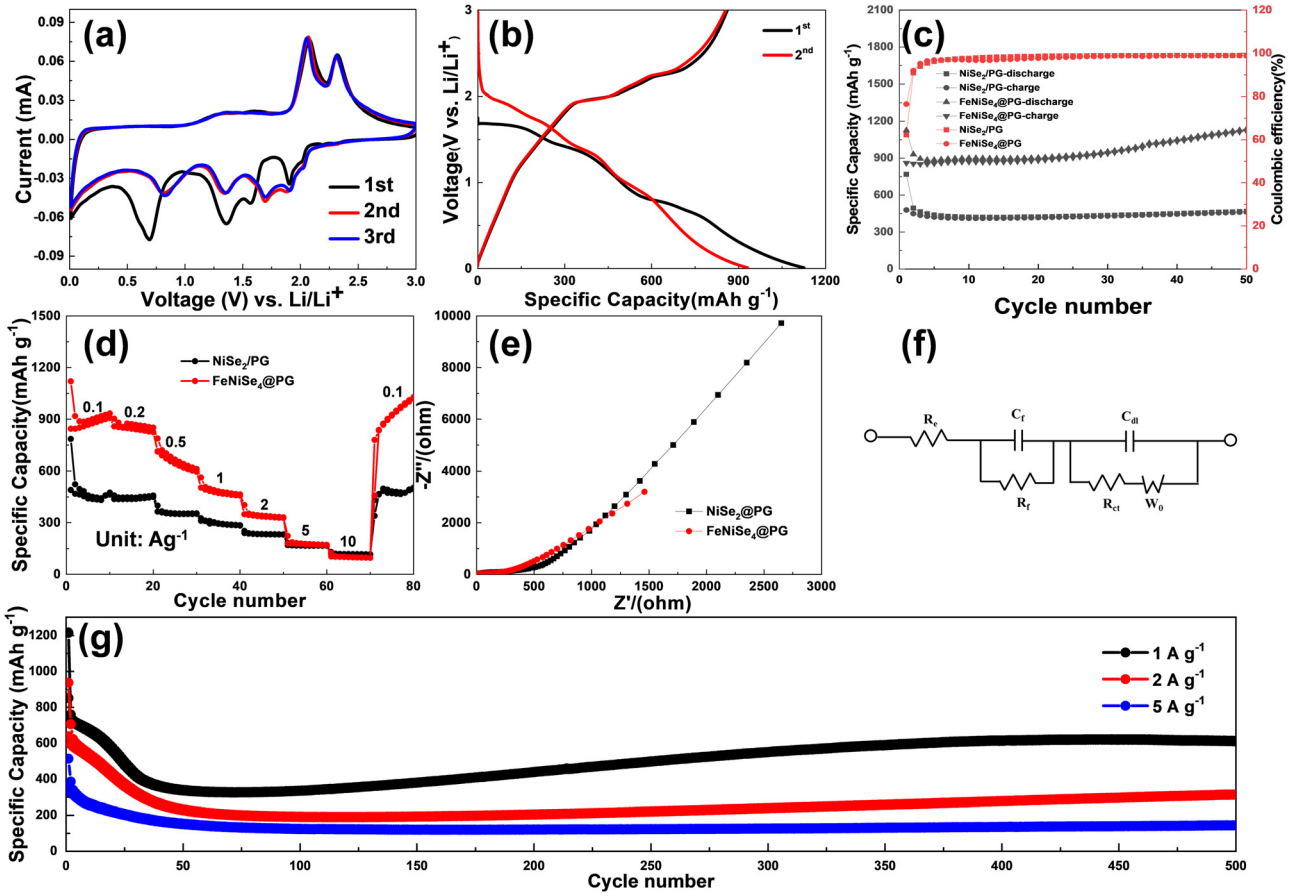

Fig. 5 (a) CV curves of the first three cycles for $FeNiSe_4$@PG; (b) initial two discharge–charge curves of $FeNiSe_4$@PG; (c) the cycle performance and coulombic efficiency of $NiSe_2$/PG and $FeNiSe_4$@PG at 100 mA g^{-1}; (d) the rate capability of $NiSe_2$/PG and $FeNiSe_4$@PG at different current densities between 0.1 and 10 A g^{-1}; (e) AC impedance spectra of $NiSe_2$/PG and $FeNiSe_4$@PG (f) the corresponding Randles equivalent circuit; and (g) the cycle performance of $FeNiSe_4$@PG at 1, 2, and 5 A g^{-1}.

one hand, the existence of irreversible capacity is due to the formation of solid electrolyte interphase (SEI) films. On the other hand, the irreversible capacity is also caused by defects and edges of porous graphene. After 50 cycles, the reversible capacity of $FeNiSe_4$@PG increased to 1121.6 mA h g^{-1}, which is higher than those of $NiSe_2$/PG (463 mA h g^{-1}) and $FeSe_2$/PG (532.1 mA h g^{-1}) (Fig. 5c and Fig. S6, ESI†). According to the TG results, the contents of graphene in $FeNiSe_4$@PG, $NiSe_2$/PG, and $FeSe_2$/PG are 76.13%, 78.18%, and 81.79%, respectively (Fig. S7, ESI†). In addition, the $FeNiSe_4$@PG electrode shows better rate capability between 0.1 and 10 A g^{-1}. The specific capacities of $FeNiSe_4$@PG at 1, 2, 5, and 10 A g^{-1} are 503.7, 349.1, 179.3, and 103.5 mA h g^{-1}, respectively. After the high rate test even at 10 A g^{-1}, when the current density returns to 100 mA g^{-1}, the specific capacity immediately returns to 779.7 mA h g^{-1}. After 80 cycles, the capacity increases to 1020.3 mA h g^{-1}, while the specific capacity of $NiSe_2$/PG was only 495.2 mA h g^{-1} (Fig. 5d).

Subsequently, the long cycle performance of the $FeNiSe_4$@PG electrode at high rates was tested as shown in Fig. 5g. At 1, 2, and 5 A g^{-1}, the first reversible capacities of $FeNiSe_4$@PG were 851.4, 639.1, and 362.1 mA h g^{-1}, and after 500 cycles, the specific capacities were still retained at 610.3, 314.1, and 144.4 mA h g^{-1}, respectively. The decrease of specific capacities during the initial few cycles is due to the poor electrolyte wetting of the $FeNiSe_4$@PG film electrode. Then, with the gradual wetting of the electrolyte, the specific capacity increases slowly and maintains stability until 500 cycles. Fig. S8a (ESI†) shows that the $FeNiSe_4$@PG electrode after cycling at 100 mA g^{-1} changed into small nanoparticles, which may lead to stronger interaction between $FeNiSe_4$ and graphene due to the more contact points. Previous studies have shown that the formation of fine particles during cycling is conducive to the promotion of reversible reaction.[59] In addition, the continuous infiltration of the electrolyte into the electrode material also contributes to the increase of capacity.[60] It is worth noting that the particle diameter of bimetallic selenide is smaller than that of monometallic selenide after cycling. Therefore, although the capacity-rise phenomenon exists in both binary-metal selenide and single-metal selenide, the capacity increase is more obvious in bimetallic selenide. Moreover, the increase is highly dependent on the current densities. Therefore, the cycled electrodes at different current densities are characterized. After cycling, the particles of the electrode materials at different current densities were agglomerated to a certain extent. The agglomerating phenomenon becomes more and more serious with the increase of current density (Fig. S9, ESI†).

To reveal the reasons for the excellent electrochemical performance of $FeNiSe_4$@PG, the electrochemical impedance spectrum was used to characterize the kinetics of $NiSe_2$/PG and $FeNiSe_4$@PG (Fig. 5e). The charge-transfer resistance of $FeNiSe_4$@PG is lower than that of $NiSe_2$/PG, indicating that the synergistic effect of the binary-metal electroactive centers can improve electrochemical reaction kinetics (Table S1, ESI†). However, the impedance was still relatively high after the addition of graphene. On the one hand, the high impedance may be due to continuous SEI formation and thickening of the SEI, which is consistent with the result that the coulomb efficiency was still less than 100% after several cycles. On the other hand, the electrode material will undergo a certain degree of volume expansion during the lithiation process, which may lead to an increase in electrode thickness, obstruction of lithium-ion diffusion, and an increase in impedance. Besides, the undesirable electrolyte decomposition may also lead to an increase in impedance.[61–63] Moreover, the diffusion coefficient of lithium ions (D_{Li^+}) for $FeNiSe_4$@PG, $NiSe_2$/PG, and $FeSe_2$/PG were investigated by the relationship between the real part of impedance (Z') and the square root of frequency ($\omega^{-1/2}$) in the low-frequency region (Fig. S10, ESI†). The slope of the fitted line represents the Warburg coefficient (σ_w), and D_{Li^+} is proportional to the $(1/\sigma_w)^2$. The D_{Li^+} of $FeNiSe_4$@PG is 3.4 and 2.0 times that of $NiSe_2$/PG and $FeSe_2$/PG, respectively, indicating better lithium-ion diffusion kinetics in $FeNiSe_4$@PG than those of $NiSe_2$/PG, and $FeSe_2$/PG.[64,65]

The relationship between the peak current (i) and the scan rate (v) can be described by the equation: $i = av^b$, where a and b are the adjustable parameters. The b-value determines the type of lithium storage behavior and can be obtained from the slope of the plot of $\log(i)$ *vs.* $\log(v)$. The b value can be used to determine whether the lithium storage behavior is diffusion-controlled ($b = 0.5$) or pseudocapacitive ($b = 1$). The b-values of peaks 1 and 2 are 0.98 and 0.89, respectively, which are very close to 1, indicating that the electrochemical reactions of $FeNiSe_4$@PG are primarily controlled by pseudocapacitance. In addition, the pseudocapacitive (k_1v) and diffusion-controlled ($k_2v^{1/2}$) contribution can be calculated by the equation of $i = k_1v + k_2v^{1/2}$, in which k_1 and k_2 can be evaluated by fitting $v^{1/2}$–$i/v^{1/2}$ plots. The pseudocapacitance contribution of the $FeNiSe_4$@PG electrode increases as the sweep rate increases, which is consistent with the b values. The pseudocapacitance contribution of $FeNiSe_4$@PG electrode at 1.2 mV s^{-1} is 82.3%, which explains the excellent rate and cycle performance (Fig. S11, ESI†).[66,67] To reveal the practicability of the binder-free $FeNiSe_4$@PG anode, a full cell was constructed and tested with $LiFePO_4$ as the cathode and $FeNiSe_4$@PG as the anode (Fig. S12, ESI†). At 0.2C, the reversible specific capacity of the full battery based on the mass of the anode is 716.5 mA h g^{-1}, which is slightly lower than the test result of the half battery, indicating that the capacity of the anode electrode can be basically utilized. Based on the total weight of the cathode and anode active material, the reversible capacity of the full battery is 86.7 mA h g^{-1} and the initial coulombic efficiency is 52%. After 50 cycles, the specific capacity can be maintained at 587.6 mA h g^{-1} and the retention rate was 82% at 0.2C, showing excellent cycle performance. On the one hand, graphene can improve the conductivity of the overall electrode material, while on the other hand, the porous structure is conducive to the infiltration of the electrolyte into the electrode material. Moreover, the porous structure can also provide more reversible reaction active sites and shorten the distance of lithium-ion diffusion. In addition, the strong interfacial interaction between $FeNiSe_4$ and graphene in $FeNiSe_4$@PG can facilitate the rapid transfer of electrons. Therefore, $FeNiSe_4$@PG shows excellent electrochemical performance when used as an anode in LIBs.

Conclusions

In summary, $FeNiSe_4$@PG was prepared by the coselenylation of iron and nickel binary-metal. $FeNiSe_4$ nanorods were anchored on the porous graphene, which can not only improve the conductivity of the electrode material but also accelerate the infiltration of electrolytes. Moreover, a porous structure can also shorten the distance of lithium-ion diffusion and electron transport. In addition, the strong interfacial interaction between porous graphene and $FeNiSe_4$ nanorods is beneficial to improving the electrochemical reactivity of $FeNiSe_4$@PG. Therefore, the $FeNiSe_4$@PG electrode material showed excellent electrochemical performance including high capacity, good rate capability, and cycle performance, when used as an anode material for LIBs.

Conflicts of interest

There are no conflicts to declare.

Acknowledgements

This work was supported by the Science and Technology Plan of Beijing Municipal Education Commission (KM202210012008), the National Key Research and Development Program of China (2022YFB3805802 and 2022YFB3805804), and the Beijing Scholars Program (RCQJ20303).

Notes and references

1 A. Kumar, B. Sah, A. R. Singh, Y. Deng, X. He, P. Kumar and R. C. Bansal, *Renewable Sustainable Energy Rev.*, 2017, **69**, 596–609.
2 J. W. Choi and D. Aurbach, *Nat. Rev. Mater.*, 2016, **1**, 16013.
3 X. Lv, W. Wei, B. Huang and Y. Dai, *J. Mater. Chem. A*, 2019, **7**, 2165–2171.
4 H. Chen, M. Zheng, S. Qian, H. Y. Ling, Z. Wu, X. Liu, C. Yan and S. Zhang, *Carbon Energy*, 2021, **3**, 929–956.
5 Z. Huang, Z. Wang, X. Wang, S. Zhang, T. Xu, Z. Zhang, J. Zang, D. Kong, X. Li and Y. Wang, *Solid State Ionics*, 2022, **380**, 115941.
6 Y. Zhong, X. Xia, F. Shi, J. Zhan, J. Tu and H. J. Fan, *Adv. Sci.*, 2016, **3**, 1500286.
7 X. Li, H. Wu, C. Guan, A. M. Elshahawy, Y. Dong, S. J. Pennycook and J. Wang, *Small*, 2019, **15**, 1803895.

8 C. Xia, Q. Jiang, C. Zhao, P. M. Beaujuge and H. N. Alshareef, *Nano Energy*, 2016, **24**, 78–86.
9 J. Huang, Z. Wei, J. Liao, W. Ni, C. Wang and J. Ma, *J. Energy Chem.*, 2019, **33**, 100–124.
10 F. Niu, J. Yang, N. Wang, D. Zhang, W. Fan, J. Yang and Y. Qian, *Adv. Funct. Mater.*, 2017, **27**, 1700522.
11 B. Zhu, D. Liu, L. Wang, B. Zhong and H. Liu, *J. Colloid Interface Sci.*, 2023, **643**, 437–446.
12 J. Ye, Z. Chen, Z. Zheng, Z. Fu, G. Gong, G. Xia and C. Hu, *J. Energy Chem.*, 2023, **78**, 401–411.
13 M. Luo, H. Yu, F. Hu, T. Liu, X. Cheng, R. Zheng, Y. Bai, M. Shui and J. Shu, *Chem. Eng. J.*, 2020, **380**, 122557.
14 B. Cong, S. Sun, B. Wang, C. Lv, J. Zhao, F. Jin, J. Jia and G. Chen, *Chem. Eng. J.*, 2022, **435**, 135185.
15 W. Zhao, Q. Tan, K. Han, D. He, P. Li, M. Qin and X. Qu, *J. Phys. Chem. C*, 2020, **124**, 12185–12194.
16 X. Zhang, J. Diao, J. Qiao, Y. Wen, H. Zhang and R. Wang, *Mater. Adv.*, 2023, **4**, 4190–4196.
17 T. Meng, Y.-N. Hao, J. Qin and M. Cao, *ACS Sustainable Chem. Eng.*, 2019, **7**, 4657–4665.
18 Z. Yan, J. Li, Q. Chen, S. Chen, L. Luo and Y. Chen, *Adv. Compos. Hybrid Mater.*, 2022, **5**, 2977–2987.
19 K. Wu, H. He, Q. Xue, C. Zhang, X. Qi, A. Cabot and X. Hu, *Chem. Eng. J.*, 2023, **466**, 142988.
20 L. Jiao, Y. Luo and L. Cheng, *Colloids Surf., A*, 2023, **664**, 131122.
21 Q. Liu, B. Chen, W. Liang, Y. Xu, G. Li, L. Shao, X. Shi and Z. Sun, *ACS Appl. Energy Mater.*, 2022, **5**, 14496–14503.
22 J. Shang, H. Dong, H. Geng, B. Cao, H. Liu, Q. Liu, X. Cao, J. Zheng and H. Gu, *Nanoscale*, 2020, **12**, 23645–23652.
23 Z. Hu, Q. Liu, S. L. Chou and S. X. Dou, *Adv. Mater.*, 2017, **29**, 1700606.
24 Z. Liang, M. Yang, S. Wang, B. Chang, H. Tu, Y. Shao, B. Zhang, H. Zhao, Y. Lei, J. Shen, Y. Wu and X. Hao, *Chem. Eng. J.*, 2021, **405**, 126724.
25 K. Jeong, J. M. Kim, S. H. Kim, G. Y. Jung, J. Yoo, S. H. Kim, S. K. Kwak and S. Y. Lee, *Adv. Funct. Mater.*, 2019, **29**, 1806937.
26 Q. Xie, P. Liu, D. Zeng, W. Xu, L. Wang, Z. Z. Zhu, L. Mai and D. L. Peng, *Adv. Funct. Mater.*, 2018, **28**, 1707433.
27 L. Zeng, Y. Fang, L. Xu, C. Zheng, M.-Q. Yang, J. He, H. Xue, Q. Qian, M. Wei and Q. Chen, *Nanoscale*, 2019, **11**, 6766–6775.
28 L. Zhou, F. Xiong, S. Tan, Q. An, Z. Wang, W. Yang, Z. Tao, Y. Yao, J. Chen and L. Mai, *Nano Energy*, 2018, **54**, 360–366.
29 S. Zhu, C. Chen, P. He, S. Tan, F. Xiong, Z. Liu, Z. Peng, Q. An and L. Mai, *Nano Res.*, 2019, **12**, 1371–1374.
30 C. Zhou, P. Zhang, J. Liu, J. Zhou, W. Wang, K. Li, J. Wu, Y. Lei and L. Chen, *J. Colloid Interface Sci.*, 2021, **587**, 260–270.
31 J. Feng, S.-h Luo, S.-x Yan, Y. Zhan, Q. Wang, Y.-h Zhang, X. Liu and L.-j Chang, *J. Mater. Chem. A*, 2021, **9**, 1610–1622.
32 S. Liu, D. Ni, H.-F. Li, K. N. Hui, C.-Y. Ouyang and S. C. Jun, *J. Mater. Chem. A*, 2018, **6**, 10674–10685.
33 H. Fan, H. Yu, X. Wu, Y. Zhang, Z. Luo, H. Wang, Y. Guo, S. Madhavi and Q. Yan, *ACS Appl. Mater. Interfaces*, 2016, **8**, 25261–25267.
34 H. Hu, J. Zhang, B. Guan and X. W. Lou, *Angew. Chem., Int. Ed.*, 2016, **55**, 9514–9518.
35 T. Yang, Y. Liu, D. Yang, B. Deng, Z. Huang, C. D. Ling, H. Liu, G. Wang, Z. Guo and R. Zheng, *Energy Storage Mater.*, 2019, **17**, 374–384.
36 F. Bonaccorso, L. Colombo, G. Yu, M. Stoller, V. Tozzini, A. C. Ferrari, R. S. Ruoff and V. Pellegrini, *Science*, 2015, **347**, 1246501.
37 Y. Shao, M. F. El-Kady, L. J. Wang, Q. Zhang, Y. Li, H. Wang, M. F. Mousavi and R. B. Kaner, *Chem. Soc. Rev.*, 2015, **44**, 3639–3665.
38 Z. Niu, P. Luan, Q. Shao, H. Dong, J. Li, J. Chen, D. Zhao, L. Cai, W. Zhou and X. Chen, *Energy Environ. Sci.*, 2012, **5**, 8726–8733.
39 T. Jin, Q. Han and L. Jiao, *Adv. Mater.*, 2020, **32**, 1806304.
40 X. Zhang, J. Zhou, X. Chen and H. Song, *ACS Appl. Energy Mater.*, 2018, **1**, 48–55.
41 X. Zhang, J. Zhou, C. Liu, X. Chen and H. Song, *J. Mater. Chem. A*, 2016, **4**, 8837–8843.
42 D. Zhou, Y. Cui, P.-W. Xiao, M.-Y. Jiang and B.-H. Han, *Nat. Commun.*, 2014, **5**, 4716.
43 R. L. Penn and J. F. Banfield, *Science*, 1998, **281**, 969–971.
44 G. Zhang, K. Liu, S. Liu, H. Song and J. Zhou, *J. Alloys Compd.*, 2018, **731**, 714–722.
45 D. Li, J. Zhou, X. Chen and H. Song, *ACS Appl. Mater. Interfaces*, 2018, **10**, 22841–22850.
46 X. Zhang, J. Zhou, H. Song, X. Chen, Y. V. Fedoseeva, A. V. Okotrub and L. G. Bulusheva, *ACS Appl. Mater. Interfaces*, 2014, **6**, 17236–17244.
47 X. Zhang, C. Liu and R. Wang, *Sustainable Energy Fuels*, 2021, **5**, 2469–2476.
48 Z. Yuan, H. Guo, Y. Huang, W. Li, Y. Liu, K. Chen, M. Yue and Y. Wang, *Chem. Eng. J.*, 2022, **429**, 132394.
49 P. Ge, H. Hou, S. Li, L. Yang and X. Ji, *Adv. Funct. Mater.*, 2018, **28**, 1801765.
50 M. Ren, H. Zang, S. Cao, H. Guo, J. Zhang, W. Liu, J.-S. Yao, X. Zhang and Z. Zhou, *J. Mater. Chem. A*, 2023, **11**, 10435–10444.
51 S. Jiang, M. Xiang, J. Zhang, S. Chu, A. Marcelli, W. Chu, D. Wu, B. Qian, S. Tao and L. Song, *Nanoscale*, 2020, **12**, 22210–22216.
52 D. Rathore, S. Ghosh, J. Chowdhury and S. Pande, *ACS Appl. Nano Mater.*, 2023, **6**, 3095–3110.
53 X. Shi, D. Lei, S. Qiao, Q. Zhang, Q. Wang, X. Deng, J. Liu, G. He and F. Zhang, *ACS Appl. Nano Mater.*, 2022, **5**, 7402–7409.
54 Z. Liang, H. Tu, K. Zhang, Z. Kong, M. Huang, D. Xu, S. Liu, Y. Wu and X. Hao, *Chem. Eng. J.*, 2022, **437**, 135421.
55 K. Srinivas, F. Ma, Y. Liu, Z. Zhang, Y. Wu and Y. Chen, *ACS Appl. Mater. Interfaces*, 2022, **14**, 52927–52939.
56 L. Yu, L. Shao, S. Wang, J. Guan, X. Shi, J. Cai, N. Tarasenko and Z. Sun, *Mater. Today Phys.*, 2022, **22**, 100593.
57 M. Ahmad, B. Xi, Y. Gu, H. Zhang and S. Xiong, *Inorg. Chem. Front.*, 2022, **9**, 448–457.
58 Y. Fang, X. Y. Yu and X. W. Lou, *Adv. Mater.*, 2018, **30**, 1706668.
59 F. Wang, R. Robert, N. A. Chernova, N. Pereira, F. Omenya, F. Badway, X. Hua, M. Ruotolo, R. Zhang and L. Wu, *J. Am. Chem. Soc.*, 2011, **133**, 18828–18836.

60 C. Masarapu, V. Subramanian, H. Zhu and B. Wei, *Adv. Funct. Mater.*, 2009, **19**, 1008–1014.
61 M. Tokur, M. Y. Jin, B. W. Sheldon and H. Akbulut, *ACS Appl. Mater. Interfaces*, 2020, **12**, 33855–33869.
62 X. Cai, L. Lai, Z. Shen and J. Lin, *J. Mater. Chem. A*, 2017, **5**, 15423–15446.
63 C. Li, X. Zhang, C. Sun, K. Wang, X. Sun and Y. Ma, *J. Phys. D: Appl. Phys.*, 2019, **52**, 143001.
64 C. Xu, T. Xia, C. Wang, Z. Li, X. Li, Y. Zhou, Y. Tang and P. Wu, *J. Power Sources*, 2022, **530**, 231290.
65 A. Zhang, Z. Fang, Y. Tang, Y. Zhou, P. Wu and G. Yu, *Nano Lett.*, 2019, **19**, 6292–6298.
66 T. Yao, H. Wang, Y. Qin, J.-W. Shi and Y. Cheng, *Composites, Part B*, 2023, **253**, 110557.
67 T. Yao, H. Wang, X. Ji, D. Wang, Q. Zhang, L. Meng, J. W. Shi, X. Han and Y. Cheng, *Small*, 2023, **19**, e2302831.